



# Analysis of Vascular Architecture and Parenchymal Damage Generated by Reduced Blood Perfusion in Decellularized Porcine Kidneys Using a Gray Level Co-occurrence Matrix

Igor V. Pantic<sup>1,2</sup>, Adeeba Shakeel<sup>3</sup>, Georg A. Petroianu<sup>4</sup> and Peter R. Corridon<sup>3,5,6,7\*</sup>

<sup>1</sup> Department of Medical Physiology, Faculty of Medicine, University of Belgrade, Belgrade, Serbia, <sup>2</sup> University of Haifa, Haifa, Israel, <sup>3</sup> Department of Pharmacology, College of Medicine and Health Sciences, Khalifa University of Science and Technology, Abu Dhabi, United Arab Emirates, <sup>4</sup> Department of Immunology and Physiology, College of Medicine and Health Sciences, Khalifa University of Science and Technology, Abu Dhabi, United Arab Emirates, <sup>5</sup> Wake Forest Institute for Regenerative Medicine, Medical Center Boulevard, Winston-Salem, NC, United States, <sup>6</sup> Biomedical Engineering, Healthcare Engineering Innovation Center, Khalifa University of Science and Technology, Abu Dhabi, United Arab Emirates, <sup>7</sup> Center for Biotechnology, Khalifa University of Science and Technology, Abu Dhabi, United Arab Emirates

## OPEN ACCESS

### Edited by:

Diego Gallo,  
Politecnico di Torino, Italy

### Reviewed by:

Breno Valentim Nogueira,  
Federal University of Espirito  
Santo, Brazil  
Maria Aurora Morales,  
National Research Council (CNR), Italy

### \*Correspondence:

Peter R. Corridon  
peter.corridon@ku.ac.ae

### Specialty section:

This article was submitted to  
Cardiovascular Imaging,  
a section of the journal  
Frontiers in Cardiovascular Medicine

**Received:** 19 October 2021

**Accepted:** 07 February 2022

**Published:** 08 March 2022

### Citation:

Pantic IV, Shakeel A, Petroianu GA  
and Corridon PR (2022) Analysis of  
Vascular Architecture and  
Parenchymal Damage Generated by  
Reduced Blood Perfusion in  
Decellularized Porcine Kidneys Using  
a Gray Level Co-occurrence Matrix.  
*Front. Cardiovasc. Med.* 9:797283.  
doi: 10.3389/fcvm.2022.797283

There is no cure for kidney failure, but a bioartificial kidney may help address this global problem. Decellularization provides a promising platform to generate transplantable organs. However, maintaining a viable vasculature is a significant challenge to this technology. Even though angiography offers a valuable way to assess scaffold structure/function, subtle changes are overlooked by specialists. In recent years, various image analysis methods in radiology have been suggested to detect and identify subtle changes in tissue architecture. The aim of our research was to apply one of these methods based on a gray level co-occurrence matrix (Topalovic et al.) computational algorithm in the analysis of vascular architecture and parenchymal damage generated by hypoperfusion in decellularized porcine. Perfusion decellularization of the whole porcine kidneys was performed using previously established protocols. We analyzed and compared angiograms of kidneys subjected to pathophysiological arterial perfusion of whole blood. For regions of interest Santos et al. covering kidney medulla and the main elements of the vascular network, five major GLCM features were calculated: angular second moment as an indicator of textural uniformity, inverse difference moment as an indicator of textural homogeneity, GLCM contrast, GLCM correlation, and sum variance of the co-occurrence matrix. In addition to GLCM, we also performed discrete wavelet transform analysis of angiogram ROIs by calculating the respective wavelet coefficient energies using high and low-pass filtering. We report statistically significant changes in GLCM and wavelet features, including the reduction of the angular second moment and inverse difference moment, indicating a substantial rise in angiogram textural heterogeneity. Our findings suggest that the GLCM method can be successfully used as

an addition to conventional fluoroscopic angiography analyses of micro/macrovascular integrity following *in vitro* blood perfusion to investigate scaffold integrity. This approach is the first step toward developing an automated network that can detect changes in the decellularized vasculature.

**Keywords:** decellularized porcine kidney, vascular architecture, parenchymal damage, gray level co-occurrence matrix algorithm, angiography, bioengineering, bioartificial kidney, decellularized kidney

## INTRODUCTION

The incidence of kidney failure, otherwise known as end-stage renal disease Zambon et al. is rising globally (1, 2). Unfortunately, there is no cure for this condition, which can develop from the progression of acute and chronic injuries (3–5). Currently, transplantation is the best option to treat ESRD. Nevertheless, very few patients receive a timely transplant due to the complexity of the procedure, lack of donors, low viability of organs, and prevailing immunological incompatibilities (6–8). As a result, there is a definite need for alternatives to address this worldwide problem. Whole organ bioengineering has been proposed as one such alternative. Major advancements in this field have been developed using three-dimensional bioprinting, advanced stem cell technologies, and organ decellularization. Among these advancements, decellularization techniques currently hold the most promise for creating a bioartificial kidney (9, 10).

Decellularization is a better alternative to porous scaffold fabrication systems, additive manufacturing procedures, and hydrogels, as it provides the necessary physical and biochemical environments to facilitate cell and tissue growth. This technology has garnered much attention within the past decade, as acellular scaffolds have been generated using bovine, equine, leporine, murine, and porcine models. However, substantial compromises to the scaffold architecture, observed under physiological conditions, inhibit their long-term viability and clinical utility (11, 12). Thus, further research is needed to overcome problems related to vascularization and help realize the promise of a bioartificial kidney (13). Using this assertion, it is necessary to devise methods to better evaluate vascular patency in post-transplantation settings. Imaging modalities like X-ray/computed tomography, magnetic resonance imaging, ultrasonography and positron emission tomography have been applied to investigate the decellularized vascular architecture (14).

Recently, our group reported the damage caused to decellularized porcine kidney scaffold vascular architecture and functionality by subjecting them to blood perfusion at pathophysiological rates using fluoroscopic angiography. We noticed substantial alterations to normal arterial branching patterns and patency, parenchymal damage, and glomerular microarchitecture disruption (12). These techniques provide useful information on the scaffold structure and function, as well as insight on the deformation that can arise after transplantation. Yet, the low spatial resolution, artifacts, and unwanted morphological alterations have always proved to be challenging to detect subtle defects (15). Such challenges

have paved the way for radiomic approaches that can extract features far beyond the capability of the human eye or brain to appreciate (16).

Computer-automated mathematical image analysis methods have emerged to give potentially wide applications in radiology. In recent years, many different techniques, and algorithms have been proposed and tested, often with limited success regarding their potential for integration in current diagnostic and research protocols. Future developments in information technology ensure that many of these techniques will significantly improve diagnostic and prognostic accuracies in X-ray computed tomography, fluoroscopy, and angiography (17–19). Computational methods that use statistical analyses in evaluating image texture are potentially instrumental in X-ray imaging since they may enable fast, objective, and accurate detection of subtle changes in tissue architecture that are occasionally hard to notice during the conventional assessment. One such method is based on the gray level co-occurrence matrix Topalovic et al. algorithm, which has attracted much attention in computational medicine. The technique uses second-order statistics to determine indicators that reflect image features such as textural homogeneity, uniformity, and level of disorder. Previously, some of these indicators, such as angular second moment and inverse difference moment, have proven to be sensitive in assessing data obtained as the result of various X-ray digital image transformations (18, 20, 21).

In angiography, GLCM was successfully used as an addition to volumetric and radiomic metrics and image reconstruction of coronary lesions (22). Also, some authors have previously demonstrated the potential of this method to evaluate endoleaks in aneurysmatic thrombus CT images of abdominal aorta (23). Endovascular aortic aneurysm repair evolution might also be indirectly assessed with the help of GLCM and other textural algorithms (24). Finally, in some experimental animal models, this form of textural analysis may be used to research pulmonary parenchymatous changes associated with pulmonary thromboembolism (25). To the best of our knowledge, no such applications of GLCM have been used in evaluating kidney vascular architecture.

The aim of our work was to apply a gray level co-occurrence matrix GLCM computational algorithm to collectively assess vascular architecture and parenchymal damage generated from hypoperfusion in decellularized porcine kidneys using fluoroscopic angiography. We present evidence that GLCM may be highly applicable in the evaluation of normal and pathological kidney angiograms indicating its potential for inclusion in contemporary research practices in this area of radiology. Also, this is the first study to quantify textural changes in vascular

architecture in decellularized kidney scaffolds, serving as the useful basis for future research on this organ model. Overall, this approach is the initial step toward developing an automated network that can detect changes in the decellularized vasculature.

## MATERIALS AND METHODS

### Experimental Animals

Adult Yorkshire pigs were euthanized, and whole kidneys were harvested under the guidelines provided by the Institutional Animal Care and Use Committee (IACUC) at the School of Medicine, Wake Forest University. All experimental protocols followed the ethical guidelines and regulations approved by Wake Forest University and the Animal Research Oversight Committee (AROC) at Khalifa University of Science and Technology, Protocol # A20-001. Moreover, all methods were performed in accordance with the Animal Research: Reporting of *In Vivo* Experiments (ARRIVE) guidelines.

### Porcine Kidney Perfusion Decellularization and Sterilization

Whole porcine kidneys were extracted with intact renal arteries, veins, and ureters. The kidneys were then decellularized and sterilized using previously established protocols (11, 12, 26). Briefly, the arteries were cannulated using PE-50 polyethylene catheter tubing (Clay Adams-Becton Dickson, Parsippany, NJ, USA) and a 14-gauge cannula and then secured with a 4/0 silk suture (Figure 1). Kidneys were flushed with 0.5–1 ml of heparinized PBS and then attached to a peristaltic pump (Cole-Palmer, Vernon Hills, IL, USA). Triton X-100, SDS, and phosphate-buffered saline (PBS) were slowly infused into cannulated renal arteries at a constant rate of 5 ml/min. Initially, 1% Triton X-100 was perfused through the renal artery for 36 h followed by 0.5% SDS dissolved in PBS for another 36 h. Finally, to remove the residual traces of detergents and cellular components, PBS was perfused through the kidneys for 72 h. The decellularized scaffolds were then submerged in PBS and sterilized with 10.0 kGy gamma irradiation.

### Blood Perfusion Studies

Blood perfusion studies were carried out as previously reported (12). Prior to perfusion, the bioreactor components, namely, suction pump heads (Ismatec, Cole-Palmer, Wertheim, Germany), standard pump tubing female and male luer x1/8" hose barb adapters, barbed fittings, reducing connectors, three-way stop cocks, and Kynar adapters (Cole-Palmer, Vernon Hills, IL, USA) were sterilized using a 60 Co Gamma Ray Irradiator. While the bioreactor tubing, chambers, and 2,000 ml round wide mouth media storage bottles with screw caps assemblies (Sigma-Aldrich, St. Louis, MO, USA) were autoclaved.

Once sterilized, the bioreactor systems were assembled within a biosafety cabinet as described earlier (12). Concisely, the chamber was assembled in a way that ensured the two outer blood flow lines were attached on either side of the suction pump head. This aided arterial outflow from the Ismatec MCP-Z Process or MCP-Z Standard programmable dispensing pump (Cole-Palmer, Vernon Hills, IL, USA) into the chamber's arterial line while the

venous returns to the pump via the venous line. The scaffold was suspended in a reservoir of roughly 500 ml of heparinized pig whole blood in the bioreactor chamber (BioIVT, Westbury, NY, USA). The renal artery was attached to the arterial line inside the chamber. In comparison, the renal vein cannula remained detached to allow venous outflow from the scaffold into the reservoir. The venous line was freely suspended into the reservoir to support unreplenished and unfiltered blood recirculation through the dispensing pumps. The entire assembled bioreactor system was then placed in a cell culture incubator, and scaffolds were subjected to continuous hypoperfusion (at a rate of 200 ml/min) for 24 h.

The pumps were set to produce pulsatile blood perfusion with 1-second fluctuations, and the model was calibrated to ensure the rotational speeds (measured in RPM) produced the desired volume flow rate of 200 ml/min. This flow rate corresponded to a perfusion pressure of 25.46 mmHg. Perfusion pressures were recorded with a digital differential pressure manometer (Dwyer Instruments, Michigan City, IN, USA) by attaching the arterial line to the manometer. At the 24-h time point, perfusion was ceased, and the scaffolds were removed from the chambers and placed in 60 × 15 mm sterilized polystyrene Petri dishes (Sigma-Aldrich, St. Louis, MO, USA) for fluoroscopic angiography.

At the 24-h time point, perfusion was ceased, and the scaffolds were removed from the chambers and placed in 60 × 15 mm sterilized polystyrene Petri dishes (Sigma-Aldrich, St. Louis, MO, USA) for fluoroscopic angiography.

### Fluoroscopic Angiography Analysis

Non-perfused ( $n = 25$ ) and hypoperfused ( $n = 25$ ) decellularized kidneys were first infused with 100 ml PBS via the renal artery. The contrast agent was infusion of Iothalamate meglumine contrast agent (60% Angio-Conray, Mallinckrodt Inc., St Louis, MO, USA). Once a sturdy flow of exiting contrast agent was achieved, the renal vein, renal artery, and ureter were occluded to prevent the contrast agent from leaking out of the organ. Angiograms were collected at ambient temperature in a sterilized suite with a Siemens C-arm Fluoroscope (Siemens AG, Munich, Germany). We measured the diameters of each major arterial branch of the renal vasculature (renal artery, segmental artery, lobar artery, interlobar artery, and arcuate artery) using ImageJ software [ImageJ 1.53 k (64-bit), US National Institutes of Health, Bethesda, MD, USA]. Specifically, three portions of each branch were randomly selected to estimate the mean diameter. Moreover, we tracked changes in the branching patterns that occurred with hypoperfusion by using the following criteria: 1° = only the renal artery was left intact; 2° = only the renal and segmental arteries were left intact; 3° = only the renal, segmental, and lobar arteries were left intact; 4° = only the renal, segmental, lobar, interlobar arteries were left intact; and 5° = all five vascular branches were left intact.

### GLCM Analysis

We performed GLCM analysis of selected regions of interest in angiograms using Mazda computational platform. This software was created by Michal Strzelecki and Piotr Szczypinski of the Institute of Electronics, Technical University of Lodz (27–29),

Poland as a part of COST B21 European project “Physiological modeling of MR Image formation,” and COST B11 AQ6 European project “Quantitative Analysis of Magnetic Resonance Image Texture” (1998–2002). The software, originally made using C++ and Delphi<sup>®</sup> programming languages can accurately calculate GLCM features on multiple regions of interest (ROIs) of high-resolution BMP images making it an ideal candidate for textural analysis of angiograms.

In our angiograms in 8-bit BMP format (bit depth equaled 24), we formed ROIs covering kidney medulla and the main elements of the vascular network, with the area of ~80,000 resolution units (width of 200 and height of 400 resolution units) as shown in **Figure 2B**. For each ROI, five major GLCM features were calculated: angular second moment, inverse difference moment, GLCLM contrast, GLCM Correlation and Sum variance of the co-occurrence matrix. GLCM method assigns values to resolution units depending on their gray intensity, after which a series of complex second-order statistical calculations are performed on resolution unit pairs considering their distance and orientation. Values of individual GLCM features depend on the distribution patterns of the gray intensity pairs and the numerical organization of the resulting co-occurrence matrix.

In GLCM analysis, angular second moment (ASM) represents the level of textural uniformity in two-dimensional signal. It can be calculated as:

$$ASM = \sum_i \sum_j \{p(i, j)\}^2$$

In this formula,  $p(i, j)$  is the  $(i, j)$  th entry of the gray-level co-occurrence matrix, after the normalization. In this work, angular second moment was in essence a tool for quantification of textural orderliness of the angiogram ROIs.

A relatively similar feature to angular second moment that can also be calculated during GLCM analysis is inverse difference moment. Inverse difference moment Maidman et al. (30) is often used to quantify the level of textural smoothness, sometimes also referred to as “homogeneity.” It can be calculated as:

$$IDM = \sum_i \sum_j \frac{1}{1 + (i - j)^2} p(i, j)$$

Some textural features take into account the mean ( $\mu$ ) and the standard deviation ( $\sigma$ ) of normalized GLCM rows (i.e.,  $x$  or  $y$ ). Such is the GLCM Correlation parameter which is determined as:

$$COR = \frac{\sum_i \sum_j (ij) p(i, j) - \mu_x \mu_y}{\sigma_x \sigma_y}$$

Textural sum variance feature is also a useful measure that can indirectly measure the level of dispersion around the mean of the matrix:

$$SVAR = \sum \left[ i - \sum p_{x-y}(i) \right]^2$$

Finally, in our study, we also quantified the textural contrast feature as:

$$CON = \sum_i \sum_j (i - j)^k P_d[i, j]^n$$

Textual contrast was used to quantify the difference between the neighboring resolution units considering their respective gray intensities.

All GLCM parameters were calculated for 4 specific pixel directions [(d,0), (0,d), (d,d), (0,-d)] at 4 different inter-pixel distances ( $d = 1-4$ ). For details on GLCM algorithm and the calculation of features, the reader is referred to previous works that deal on the application of this method in medical and other sciences (31–33).

## Discrete Wavelet Transform Features

Discrete wavelet transform (DWT) analysis of angiogram ROIs was performed as an addition to calculation of GLCM features. The DWT algorithm in Mazda software includes linear transformation of data vectors to numerical vectors taking into account their lengths (in case of data vectors, the length of an integer power of two). The analysis is performed separately on rows and columns of data with the application of high (H) and low-pass (L) filtering (34). The final output of DWT includes energies ( $E_n$ ) of wavelet coefficients ( $d$ ) in different subbands (for a respective subband location  $x$  and  $y$ ) at different scales for a ROI resolution unit number ( $n$ ):

$$E = \frac{\sum_{x,y \in ROI} (d_{x,y}^{subband})^2}{n}$$

Previous research on application of DWT in microscopy has indicated that textural heterogeneity may influence the values of coefficient energies in subbands. In this work, we focused on the quantification of 3 such energies depending on the use of high (H) and low-pass (L) filtering: EnLH, EnHL and EnHH. Additional details on DWT algorithm can be found in previous publications (34, 35).

## Statistical Analysis

Non-parametric statistics were applied to analyze the data using SPSS v.25.0 (IBM Corporation, Chicago, IL). We used the Kruskal–Wallis one-way analysis of variance Ucci et al. (36) with the *post hoc* Dunn’s test to compare the arterial diameters of the renal artery (RA), segmental artery (SA), lobar artery (LA), interlobar artery (IA), and arcuate artery Periyah et al. in both non-perfused and hypoperfused scaffolds. The comparison between the diameters of non-perfused and hypoperfused scaffolds was done using the Mann-Whitney  $U$ -test. Difference in GLCM and DWT values between non-perfused and hypoperfused decellularized kidneys were also evaluated using Mann-Whitney  $U$  and Kruskal–Wallis tests. A two-tailed  $p$ -value  $< 0.05$  was considered to be statistically significant.

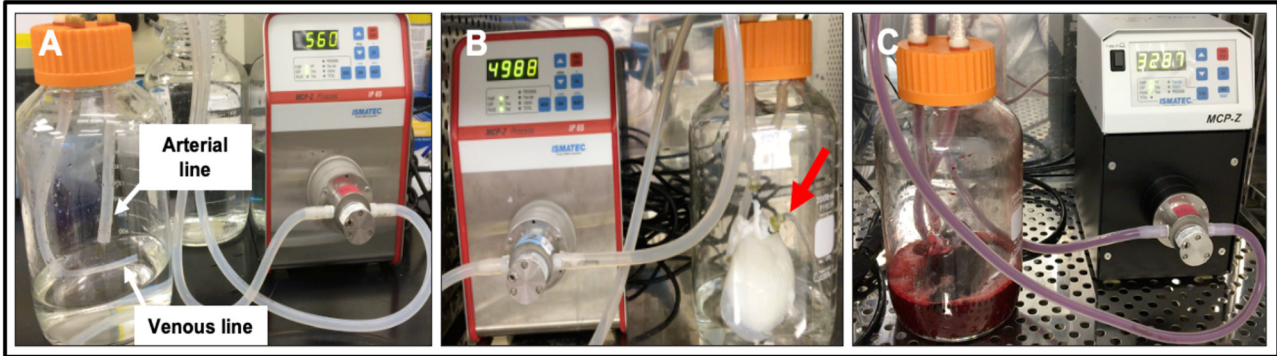


**FIGURE 1** | Photographs of the bioreactor used to perfuse decellularized scaffolds with whole blood. **(A)** Image outlining the arterial line (which was then attached to the cannulated renal artery) and venous lines (which was left open to act as a venous reservoir to facilitate fluid recirculation) before the addition of the scaffold. **(B)** Image of an acellular kidney perfused with PBS illustrates how the scaffold recirculated fluid that emanated from its renal vein (red arrow) and open-ended venous line. **(C)** Image of a scaffold being perfused with whole pig blood.

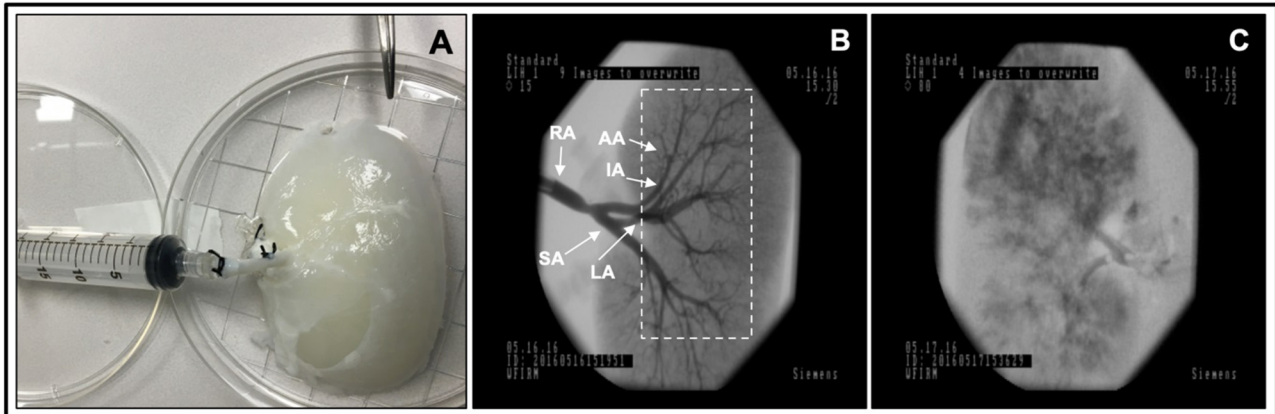


**FIGURE 2** | Fluoroscopic angiography. **(A)** Photograph of a decellularized scaffold that was set to be infused with contrast agent. **(B)** An angiogram of the scaffold before it was perfused with blood displaying the decellularized vascular network and region of interest Davidovic et al., dashed rectangular region, covering kidney medulla and the main elements of this network. **(C)** An angiogram of the scaffold after 24 h of hypoperfusion (arterial infusion rate 20 ml/min). The major arterial branches of the renal vasculature are defined as follows, RA, renal artery; SA, segmental artery; LA, lobar artery; IA, interlobar artery; and AA, arcuate artery.

## RESULTS

### Scaffold Perfusion Analyzed Using Fluoroscopic Angiography and Venous Outflow

Fluoroscopic angiography showed that the vascular network was well-preserved post decellularization in non-perfused kidneys (**Figure 2B**). Angiograms taken from decellularized kidneys post-perfusion with unreplenished and unfiltered blood for 24 h revealed alterations in the decellularized vascular architecture and parenchyma (**Figure 2C**). Substantial levels of contrast agent extravasation were also observed throughout the cortical and medulla regions highlighting deleterious modifications to the integrity of decellularized renal parenchyma. Moreover, the hypoperfused acellular kidneys were unable to perfuse blood throughout their vascular networks and showed notable signs of thrombosis and cessation of venous outflow.

Furthermore, we observed considerable reductions in the diameter of each vascular segment (**Figure 3**), apart from the arcuate arterial track, within hypoperfused scaffolds. Angiographic analyses also revealed substantial disruptions to the branching patterns observed within these hypoperfused kidneys. The typical branching pattern ( $5^\circ$ ) was maintained in non-perfused kidneys, whereas hypoperfused kidneys displayed patterns that ranged from  $5^\circ$  to  $1^\circ$  (**Figure 4**). Specifically, the standard arterial branching patterns were noticeably disrupted by the end of perfusion, making it difficult to detect and differentiate the various branches of the arterial tree.

Kruskal–Wallis one-way analysis of variance Ucci et al. identified differences in the mean diameters of arterial branches, namely, renal artery (RA), segmental artery (SA), lobar artery (LA), interlobar artery (IA), and arcuate artery Periyah et al. in both non-perfused ( $p < 0.001$ ) and hypoperfused ( $p < 0.001$ ) scaffolds, individually. The *post hoc* Dunn's test applied to the

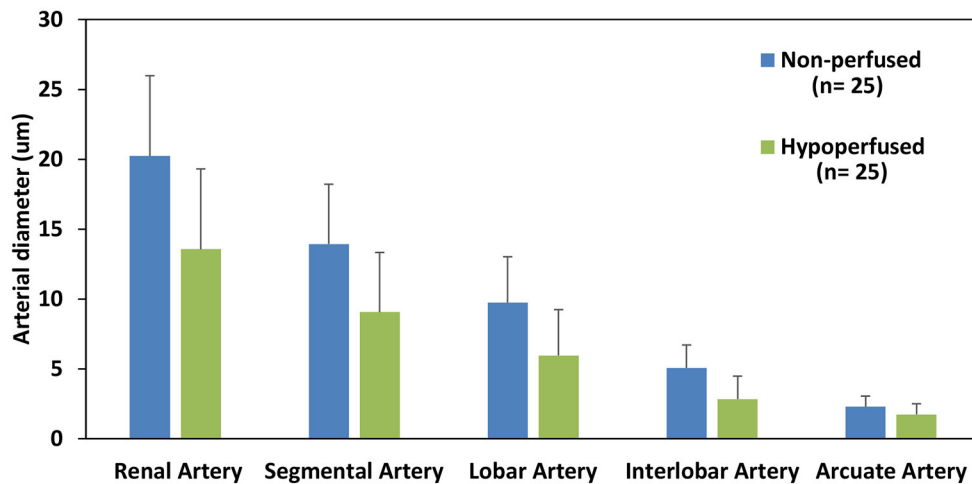


**FIGURE 3** | Estimated diameters of each major arterial branch of the renal vasculature. A comparison of the diameters of the major arterial branch of the renal vasculature in non-perfused and hypoperfused decellularized kidneys.

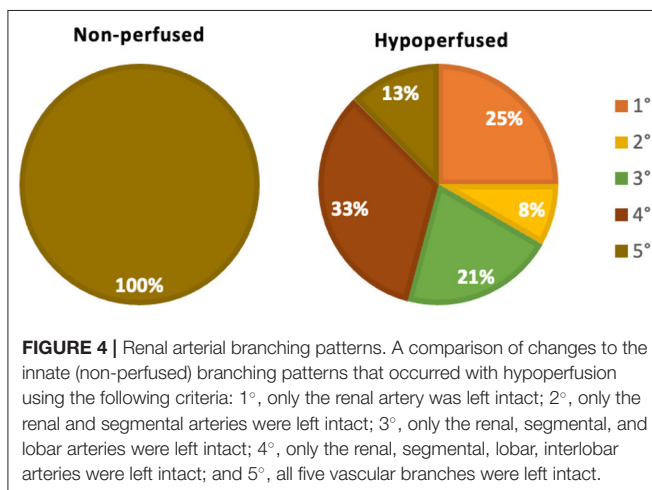


**FIGURE 4** | Renal arterial branching patterns. A comparison of changes to the innate (non-perfused) branching patterns that occurred with hypoperfusion using the following criteria: 1°, only the renal artery was left intact; 2°, only the renal and segmental arteries were left intact; 3°, only the renal, segmental, and lobar arteries were left intact; 4°, only the renal, segmental, lobar, interlobar arteries were left intact; and 5°, all five vascular branches were left intact.

non-perfused decellularized data showed significant differences ( $p < 0.05$ ) among the mean diameters of almost all pairs of branches except for SA-RA ( $p = 0.63$ ) and AA-IA ( $p = 0.13$ ). For the hypoperfused decellularized samples, the *post hoc* Dunn's pairwise test also revealed significant differences in the mean diameters for almost all the major arterial branches except for AA-IA ( $p = 0.5$ ), IA-LA ( $p = 0.065$ ), and LA-SA ( $p = 0.05$ ).

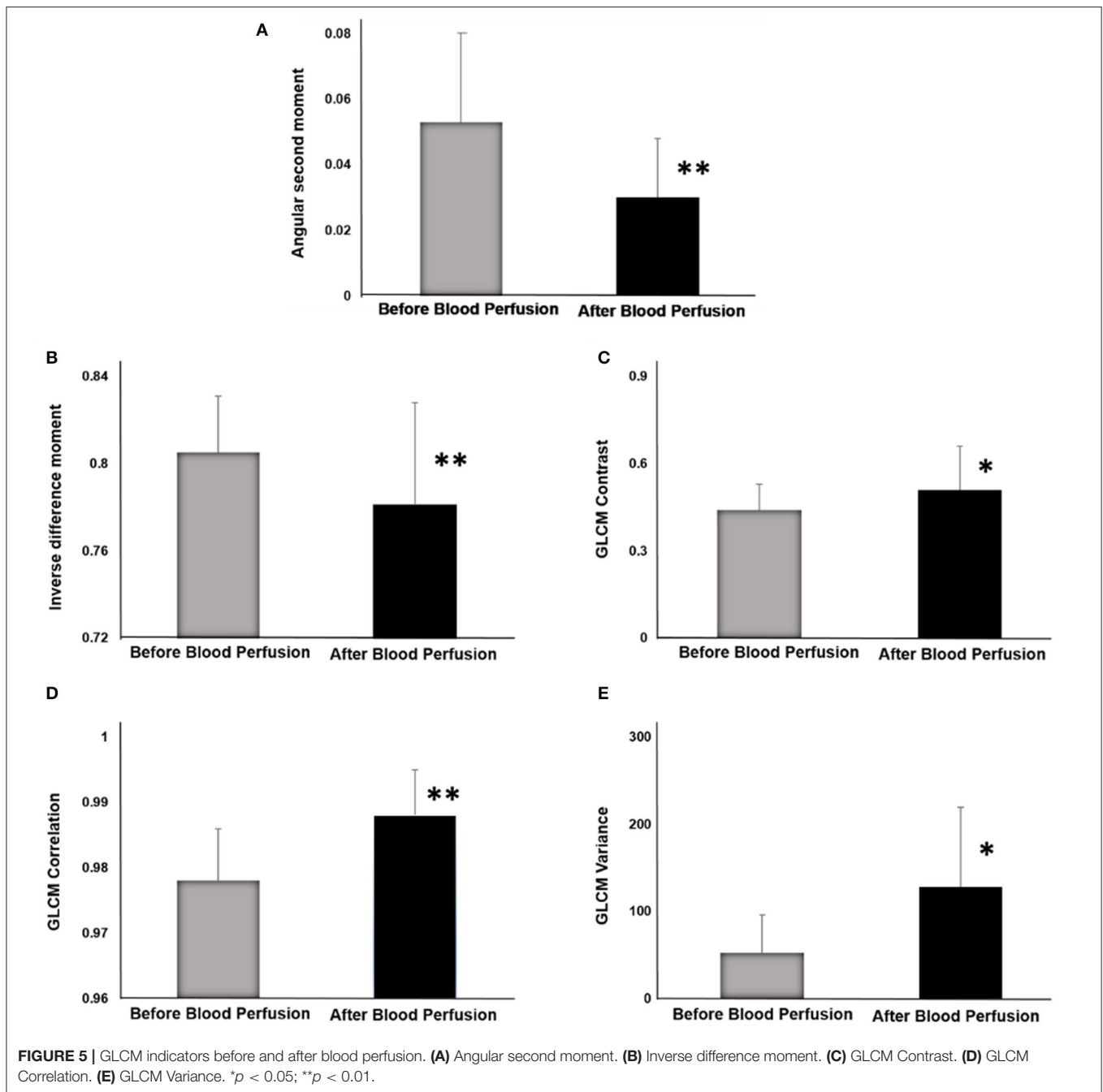
Moreover, the Mann-Whitney  $U$ -test was used to compare the diameters of the various arterial branches of non-perfused and hypoperfused scaffolds. There were significant decreases ( $p < 0.05$ ) in the diameter of the arterial branches in hypoperfused scaffolds as compared to non-perfused scaffolds, except for reductions observed between arcuate arteries of the two groups ( $p = 0.342$ ).

## GLCM Analysis

For the inter-pixel distance of 1 and direction (1,0), the average angular second moment of the ROIs was  $0.053 \pm 0.022$  for decellularized kidneys before perfusion (pre-perfusion) and  $0.030 \pm 0.018$  for after perfusion (post post-perfusion) angiograms (**Figure 5A**). Statistically highly significant difference was observed ( $p < 0.01$ ). This result implied a substantial reduction of textural uniformity in post-perfusion vascular architecture. Similar reduction was observed with the mean values of inverse difference moment ( $0.781 \pm 0.046$  in post-perfusion compared to  $0.805 \pm 0.026$  in controls) (**Figure 5B**). The difference was highly significant ( $p < 0.05$ ) which implied that the textural homogeneity of ROIs decreased.

On the other hand, there was a substantial rise in the average values of GLCM Contrast (**Figure 5C**), GLCM Correlation feature (**Figure 5D**) and Sum variance (**Figure 5E**). The largest increase was observed in Sum variance ( $127.99 \pm 91.53$  in post-perfusion vs.  $52.48 \pm 43.36$  in pre-perfusion angiograms,  $p < 0.01$ ) followed by the Correlation ( $0.989 \pm 0.007$  vs.  $0.978 \pm 0.008$ ,  $p < 0.01$ ), and lastly GLCM Contrast ( $0.51 \pm 0.15$  vs.  $0.44 \pm 0.09$ ,  $p < 0.05$ ). This is in line with the results of the values of angular second moment and inverse difference moment, and imply the rise of the overall textural heterogeneity of vascular architecture. Average values and standard deviations (SD) of GLCM parameters before and after perfusion (per) for specific interpixel distances (d) and directions (dir) are presented in **Table 1**.

We also observed some changes in wavelet coefficient energies of the ROIs, however these changes were not as drastic as the ones exhibited by GLCM features. The average value of EnLH rose from  $1.17 \pm 0.45$  in controls to  $1.54 \pm 0.70$  in post-perfusion angiograms ( $p < 0.05$ ). Similar rise and level of significance was observed for EnHL means ( $1.07 \pm 0.36$  compared to  $1.37 \pm 0.53$  in controls,  $p < 0.05$ ). Regarding EnHH, the average value in



pre-perfusion angiograms was  $0.08 \pm 0.01$  and in post-perfusion angiograms it rose to  $0.09 \pm 0.02$  ( $p > 0.05$ ).

Significant correlations were detected between GLCM and DWT parameters in both groups of angiograms. For example, statistically highly significant negative correlation ( $p < 0.01$ ) existed between the DWT EnHL feature and the values of inverse difference moment. Similar statistically highly significant negative correlation ( $p < 0.01$ ) was observed between EnHH feature and the values of angular second moment. These associations are expected, they are partly the result of the methodological similarities during the implementation of

GLCM and DWT algorithms, and confirm the validity of the obtained dataset.

## DISCUSSION

Time and again, emphasis has been given to the importance of maintaining the integrity of vascular networks in decellularized organs for transplantation. These vascular tracks support the homogenous recellularization process in complex organs like the kidney. It is vital to consider the infusion rate, volume, and cell

**TABLE 1** | Average values and standard deviations (SD) of GLCM indicators before and after perfusion (per) for specific interpixel distances (d) and directions (dir).

d	dir	per	ASM	ASM SD	CON	CON SD	COR	COR SD	IDM	IDM SD	SVAR	SVAR SD
1	(1,0)	before	0.053	0.022	0.44	0.09	0.978	0.008	0.805	0.026	52.5	43.3
		after	0.030**	0.018	0.51*	0.15	0.99	0.007	0.781**	0.047	128.0**	91.5
	(0,1)	before	0.056	0.023	0.46	0.12	0.978	0.009	0.816	0.027	52.6	43.5
		after	0.031**	0.018	0.54*	0.18	0.988**	0.006	0.796*	0.044	128.4**	91.9
	(1,1)	before	0.043	0.018	0.71	0.21	0.965	0.013	0.742	0.032	52.1	43.1
		after	0.024**	0.016	0.85*	0.29	0.982**	0.010	0.714**	0.058	127.4**	91.2
	(1,-1)	before	0.043	0.018	0.72	0.20	0.965	0.013	0.741	0.033	52.1	43.1
		after	0.024**	0.016	0.87*	0.31	0.981**	0.010	0.712**	0.059	127.4**	91.2
2	(2,0)	before	0.036	0.016	1.05	0.36	0.950	0.017	0.680	0.042	51.6	42.8
		after	0.020**	0.014	1.33*	0.50	0.972**	0.014	0.641**	0.070	126.5**	90.6
	(0,2)	before	0.038	0.017	1.16	0.44	0.945	0.019	0.689	0.040	51.8	43.1
		after	0.020**	0.014	1.39	0.57	0.972**	0.013	0.654*	0.066	127.3**	91.4
	(2,2)	before	0.030	0.014	1.81	0.79	0.916	0.028	0.610	0.046	50.7	42.2
		after	0.016**	0.012	2.28*	0.96	0.954**	0.020	0.565**	0.077	125.1**	89.9
	(2,-2)	before	0.030	0.014	1.85	0.73	0.913	0.027	0.609	0.047	50.7	42.3
		after	0.016**	0.011	2.35	1.03	0.953**	0.021	0.562**	0.077	125.1**	89.9
3	(3,0)	before	0.031	0.015	1.77	0.78	0.919	0.024	0.611	0.054	50.7	42.2
		after	0.016**	0.012	2.35*	1.01	0.953**	0.021	0.557**	0.080	124.8**	89.6
	(0,3)	before	0.030	0.014	2.02	0.93	0.907	0.031	0.608	0.049	50.9	42.5
		after	0.016**	0.011	2.45	1.11	0.952**	0.020	0.562**	0.076	126.1**	90.8
	(3,3)	before	0.026	0.013	3.03	1.63	0.864	0.041	0.546	0.056	49.2	41.1
		after	0.013**	0.010	3.93*	1.82	0.923**	0.029**	0.485**	0.082	122.7**	88.4
	(3,-3)	before	0.025	0.013	3.08	1.45	0.860	0.041	0.544	0.057	49.2	41.3
		after	0.012**	0.009	4.06*	1.95	0.921**	0.031**	0.483**	0.083	122.5**	88.4
4	(4,0)	before	0.027	0.014	2.53	1.29	0.887	0.031	0.567	0.063	49.7	41.5
		after	0.013**	0.010	3.50*	1.62	0.932**	0.027**	0.501**	0.085	123.1**	88.5
	(0,4)	before	0.026	0.013	2.96	1.52	0.867	0.043	0.558	0.056	49.9	41.9
		after	0.013**	0.009	3.66	1.74	0.930**	0.027**	0.502**	0.080	124.7**	90.1
	(4,4)	before	0.023	0.012	4.22	2.54	0.814	0.054	0.509	0.063	47.8	39.9
		after	0.011**	0.008	5.66*	2.77	0.891**	0.038**	0.435**	0.084	120.1**	86.9
	(4,-4)	before	0.023	0.012	4.26	2.20	0.810	0.052	0.508	0.064	47.8	40.2
		after	0.011**	0.008	5.84*	2.94	0.888**	0.040**	0.433**	0.084	120.0**	86.9

\* $p < 0.05$ ; \*\* $p < 0.01$ .

type to ensure that the repopulation process does not constrict vascular ducts. Another consideration is the effective removal of the detergents after decellularization. Ineffective removal would prolong the decellularization process and favor disruption of the ECM, and previous studies have shown that SDS and Triton X-100 can denature the triple-helical collagen structure (37, 38). Thus, it is crucial to understand the various conditions that lead to scaffold damage entirely. Such an improved understanding will help us develop enhanced scaffolds that may be able to withstand the recellularization process better and support the development of bioartificial organs.

To better understand these processes, we subjected decellularized scaffolds to hypoperfused infusion rates. Hypoperfusion substantially affected the vascular architecture of the decellularized kidney. For instance, platelet activation and coagulation usually do not occur within the intact vasculature. However, without an intact endothelium and a reduced perfusion

rate, the whole blood would have been in direct contact with collagen for substantial periods. As a result, platelets would have been in direct contact with collagen fibers within the scaffold and enabled their adhesion and aggregation (39). This highly thrombogenic environment generated within the decellularized vasculature would have thus supported the development of vascular occlusions throughout the scaffold. Such occlusions would have increased blood viscosity, reduced flow rates, and facilitated the accumulation of viscous blood in the kidney over time, resulting in hemostasis and swelling. These events could explain the substantial disruptions to the scaffold parenchyma observed in the decellularized kidneys (12).

From our analyses, we observed significant decreases in the diameters of the major arterial branches in hypoperfused scaffolds compared to the non-perfused scaffolds. We then applied textural analysis algorithms based on gray level co-occurrence matrix and discrete wavelet transform to investigate

the pathologically changes in the vascular architecture of the decellularized kidneys subjected to conditions that mimic renal artery stenosis (12). This form of stenosis is a well-recognized disorder that compromises transplantation and has been shown to denature the acellular vascular tracks. Such deformation also leads to aberrant changes in the decellularized parenchyma. The images obtained using fluoroscopic angiography showed that significant differences in both GLCM and DWT features could be detected using this approach.

With respect to textural analysis, as reported in the previously published studies, we can assume that GLCM parameters are potentially useful indicators of discrete changes in tissue architecture (40). In tissue micrographs, this has been shown to be the case in both physiological and pathological conditions (41, 42). The reduction of angular second moment (textural uniformity) and inverse difference moment (textural homogeneity) might be related to parenchymal structural degradation and deterioration as suggested earlier (40). In general, previous research has shown that in parenchymatous organs, these GLCM parameters decrease as the level of entropy (degree of structural chaos and disorder) increases (43). As for the GLCM contrast and GLCM correlation, in micrographs, these parameters showed relatively good discriminatory power in differentiating between healthy kidney medular tissue and the tissue following reperfusion injury (40). In our current research, since the analysis was done following the process of decellularization, we can speculate that the ASM and IDM reductions were associated with the changes in vascular network patterns, possibly due to the structural damage of blood vessels. Also, hypoperfusion-related clotting, as well as structural deterioration of extracellular and extravascular matrix might also have significantly contributed to the observed changes in GLCM parameters. Nevertheless, it should be noted that GLCM analysis is a relatively new method in both biology and radiology and additional research is needed to draw definite conclusions on the relationship between specific structural changes in kidney tissue and changes in GLCM parameters. Our findings imply that textural analysis, as a set of contemporary computer-based methods, has a great potential to be used as an addition to the conventional angiographic evaluation of the renal vascular network.

Perhaps the most important finding was the observed significant change of inverse difference moment of angiogram ROIs. This GLCM feature indicates textural homogeneity and is often used to quantify smoothness in the distribution of resolution units in grayscale images. Previous research articles in digital micrographs have shown the potential value of inverse difference moment in detecting structural alterations that are not visible to a professional pathologist (35, 44).

Along with angular second moment and GLCM contrast, this is probably also one of radiology's most frequently calculated textural features.

Generally, in the past, the most frequent application of textural computational algorithms in radiology was to assess images obtained through nuclear magnetic resonance, computerized tomography, and other tomography techniques. Probably the most common approach is to compare the images of tissue

lesions or other pathological changes in tissue architecture with controls. After that, one of the possibilities is to determine the sensitivity of individual GLCM features for lesion detection or to test the discriminatory power of the method regarding the separation of post- and pre-perfusion radiographs or parts of a radiograph (20). Another strategy would be to use GLCM features as prediction tools for disease prognosis (45), or to test their ability to determine boundaries of the lesion in the same radiograph. Finally, it may be possible to develop a scoring system that considers GLCM (and other) indicators of texture and test its sensitivity and specificity (46).

In angiography, the GLCM method is much less frequently applied, and so far, only a handful of studies have been published on this topic. These mainly include the use of GLCM features for assessment of low attenuation non-calcified (LANCP), non-calcified and calcified coronary plaques (18, 22), or for computer-aided diagnosis-specific cases of endovascular aortic aneurysms (24). In optical coherence tomography angiography, as demonstrated earlier, some GLCM indicators can also be applied to quantify choriocapillaris in healthy and diseased eyes (47). To the best of our knowledge, there hasn't been a similar study trying to apply texture analysis for the assessment of vascular changes in kidney tissue. Therefore, our research is probably the first to demonstrate the applicability of these computational algorithms (GLCM and DWT techniques on an experimental model of decellularized kidney) in this rapidly developing area of radiology and also provides a potentially useful foundation for future research.

In the future, probably the most important application of both GLCM and DWT analyses will be to provide inputs for various artificial intelligence-based methods for image analysis in radiology. This application would include training and testing different machine learning models, some of which have already been suggested as suitable for GLCM data (44). The examples would be conventional decision tree algorithms such as CHAID (Chi-square Automatic Interaction Detector) or CART (classification and regression tree) or some more modern approaches such as random forests. Support vector machines, naive Bayes, linear discriminant analysis, and similarity learning are potential alternative strategies. The most considerable potential regarding the use of GLCM and DWT raw data may lie in designing various types of neural networks. This process includes simple concepts such as a multilayer perceptron or more complex ones such as recurrent and convolutional neural networks. Convolutional neural networks are a fascinating approach since they are already widely used in medicine and other disciplines of computer vision. Despite the promises that such a computer algorithm makes, many loopholes still need to be addressed that will require extensive quality assurance of these methods, including testing inter- and intra-observer reliability, for their effective application in the clinics.

As mentioned, the limitations of our study include the relatively small sample, which is not sufficient for the implementation of the more complex approaches such as machine learning or the creation of other artificial intelligence-based models. Also, another important aspect to consider is that the results of GLCM and DWT generally depend on various

factors associated with image creation. Brightness, contrast, hue, saturation, and many other image parameters which can vary in angiograms can substantially impact GLCM features such as angular second moment or inversed difference moment.

Another important limitation is that the fact that the results of GLCM and DWT analyses in certain circumstances may greatly vary and depend on the positioning of the region of interest within the image. In our study we positioned the ROI to always cover the same area of the kidney, with the left boundary in the proximate vicinity to the area where the branches of the renal artery appear to enter the hilum. Although in our study we successfully applied this approach in all angiograms, in the future it may not be always feasible due to radiological and other factors. Future studies will have to additionally validate this strategy and perform a comprehensive quality assurance of both GLCM and DWT techniques and their applications in renal angiography.

Finally, to our knowledge, the results of the textural analysis are not always the same across different computational platforms. Such variations can arise from the fact that existing software algorithms may use images in different formats (8-bit, 16-bit, BMP, JPG, etc.) or because of many other technical issues and solutions the developers tried to include into the programming code. All of these issues may in the future hinder the potential of successful integration of textural analysis methods in contemporary diagnostic protocols. For this to happen, extensive quality assurance of the processes, including testing inter- and intra-observer reliability, will have to be performed.

## CONCLUSION

Our results designate that certain discrete changes in vascular architecture and renal parenchyma in the decellularized kidney can be successfully detected using well-known contemporary computational algorithms for texture analysis, thereby overcoming the limitations of conventional imaging modalities. We report statistically significant changes in GLCM and wavelet features, including reducing angular second moment and inverse difference moment, indicating a substantial rise in angiogram textural heterogeneity in pathological conditions. Our findings suggest that the GLCM method may be used as an addition to the conventional fluoroscopic angiography analysis of micro-/macrovascular integrity for a more accurate diagnosis. To the best of our knowledge, this is the first study to use GLCM and DWT based approach in decellularized kidney experimental model, augmenting appropriate evaluation of

the decellularized kidneys vasculature, to accomplish lasting vascular patency post-transplantation, thereby giving hope to impede a looming epidemic of morbidity or mortality due to kidney diseases. This approach is the first step toward developing an automated network that can detect debilitating changes in the decellularized vasculature and supporting tissue network.

## DATA AVAILABILITY STATEMENT

The raw data supporting the conclusions of this article will be made available by the authors, without undue reservation.

## ETHICS STATEMENT

The animal study was reviewed and approved by Institutional Animal Care and Use Committee (IACUC) at the School of Medicine, Wake Forest University; Animal Research Oversight Committee (AROC) at Khalifa University of Science and Technology.

## AUTHOR CONTRIBUTIONS

PC and IP conceived and designed project. PC performed all experiments, analyzed the associated data, and interpreted results of experiments. IP performed all computation analyses. IP, AS, GP, and PC drafted, edited, and approved final version of manuscript. All authors contributed to the article and approved the submitted version.

## FUNDING

This study was supported in part by an Institutional Research and Academic Career Development Award (IRACDA), Grant No. NIH/NIGMS K12-GM102773, and funds from Khalifa University of Science and Technology, Grant Nos. FSU-2020-25 and RC2-2018-022 (HEIC).

## ACKNOWLEDGMENTS

The author would like to acknowledge Dr. Zambon for help with decellularization. The authors would also like to thank Ms. Anousha Khan, Ms. Xinyu Wang, and Nnamdi Ugwuoke for reviewing the manuscript.

## REFERENCES

1. Arikian H, Ozturk S, Tokgoz B, Dursun B, Seyahi N, Trabulus S, et al. Characteristics and outcomes of acute kidney injury in hospitalized COVID-19 patients: a multicenter study by the Turkish society of nephrology. *PLoS ONE*. (2021) 16:e0256023. doi: 10.1371/journal.pone.0256023
2. Kari JA, Shalaby MA, Albanna AS, Alahmadi TS, Alherbish A, Alhasan KA. Acute kidney injury in children with COVID-19: a retrospective study. *BMC Nephrol*. (2021) 22:202. doi: 10.1186/s12882-021-02389-9
3. Hsu RK, Hsu CY. The role of acute kidney injury in chronic kidney disease. *Semin Nephrol*. (2016) 36:283–92. doi: 10.1016/j.semnephrol.2016.05.005
4. Kolb AL, Corridon PR, Zhang S, Xu W, Witzmann FA, Collett JA, et al. Exogenous gene transmission of isocitrate dehydrogenase 2 mimics ischemic preconditioning protection. *J Am Soc Nephrol*. (2018) 29:1154–64. doi: 10.1681/ASN.2017060675
5. Corridon PR, Karam SH, Khraibi AA, Khan AA, Alhashmi MA. Intravital imaging of real-time endogenous actin dysregulation in proximal and distal tubules at the onset of severe ischemia-reperfusion injury. *Sci Rep*. (2021) 11:8280. doi: 10.1038/s41598-021-87807-6
6. Saidi RF, Hejazii Kenari SK. Challenges of organ shortage for transplantation: solutions and opportunities. *Int J Organ Transplant Med*. (2014) 5:87–96.
7. Job K, Antony A. *Organ Donation and Transplantation: "Life after Death"* London: IntechOpen (2018).

8. Wu H, Lau ESH, Yang A, Szeto CC, Ma RCW, Kong APS, et al. Trends in kidney failure and kidney replacement therapy in people with diabetes in Hong Kong, 2002-2015: a retrospective cohort study. *Lancet Reg Health West Pac.* (2021) 11:100165. doi: 10.1016/j.lanwpc.2021.100165
9. Corridon PR, Ko IK, Yoo JJ, Atala A. Bioartificial kidneys. *Curr Stem Cell Rep.* (2017) 3:68–76. doi: 10.1007/s40778-017-0079-3
10. Sohn S, Buskirk M, Buckenmeyer M, Londono R, Faulk D. Whole organ engineering: approaches, challenges, future directions. *Appl Sci.* (2020) 10:4277. doi: 10.3390/app10124277
11. Zambon JP, Ko IK, Abolbashari M, Huling J, Clouse C, Kim TH, et al. Comparative analysis of two porcine kidney decellularization methods for maintenance of functional vascular architectures. *Acta Biomater.* (2018) 75:226–34. doi: 10.1016/j.actbio.2018.06.004
12. Corridon PR. In vitro investigation of the impact of pulsatile blood flow on the vascular architecture of decellularized porcine kidneys. *Sci Rep.* (2021) 11:16965. doi: 10.1038/s41598-021-95924-5
13. Feng H, Xu Y, Luo S, Dang H, Liu K, Sun WQ. Evaluation and preservation of vascular architectures in decellularized whole rat kidneys. *Cryobiology.* (2020) 95:72–79. doi: 10.1016/j.cryobiol.2020.06.003
14. Huling JC, Atala A, Yoo JJ. Chapter 42 - decellularized whole organ scaffolds for the regeneration of kidneys. In: Little MH, editors. *Kidney Development, Disease, Repair and Regeneration.* San Diego: Academic Press (2016). p. 569–78.
15. Mostaco-Guidolin LB, Ko AC, Wang F, Xiang B, Hewko M, Tian G, et al. Collagen morphology and texture analysis: from statistics to classification. *Sci Rep.* (2013) 3:2190. doi: 10.1038/srep02190
16. Neri E, de Souza N, Brady A, Bayarri AA, Becker CD, Coppola F, et al. What the radiologist should know about artificial intelligence – an ESR white paper. *Insights Imag.* (2019) 10:44. doi: 10.1186/s13244-019-0738-2
17. Cao W, Pomeroy MJ, Gao Y, Barish MA, Abbasi AF, Pickhardt PJ, et al. Multi-scale characterizations of colon polyps via computed tomographic colonography. *Vis Comput Ind Biomed Art.* (2019) 2:25. doi: 10.1186/s42492-019-0032-7
18. Kolossvary M, Javorszky N, Karady J, Vecsey-Nagy M, David TZ, Simon J, et al. Effect of vessel wall segmentation on volumetric and radiomic parameters of coronary plaques with adverse characteristics. *J Cardiovasc Comput Tomogr.* (2021) 15:137–45. doi: 10.1016/j.jcct.2020.08.001
19. Gudigar A, Raghavendra U, Hegde A, Menon GR, Molinari F, Ciaccio EJ, et al. Automated detection and screening of traumatic brain injury (TBI) using computed tomography images: a comprehensive review and future perspectives. *Int J Environ Res Public Health.* (2021) 18:6499. doi: 10.3390/ijerph18126499
20. Chen H, Li W, Zhu Y. Improved window adaptive gray level co-occurrence matrix for extraction and analysis of texture characteristics of pulmonary nodules. *Comput Methods Programs Biomed.* (2021) 208:106263. doi: 10.1016/j.cmpb.2021.106263
21. Shankar K, Perumal E, Tiwari P, Shorfuzzaman M, Gupta D. Deep learning and evolutionary intelligence with fusion-based feature extraction for detection of COVID-19 from chest X-ray images. *Multimed Syst.* (2021) doi: 10.1007/s00530-021-00800-x. [Epub ahead of print].
22. Kolossvary M, Szilveszter B, Karady J, Drobni ZD, Merkely B, Maurovich-Horvat P. Effect of image reconstruction algorithms on volumetric and radiomic parameters of coronary plaques. *J Cardiovasc Comput Tomogr.* (2019) 13:325–30. doi: 10.1016/j.jcct.2018.11.004
23. Garcia G, Maiora J, Tapia A, De Blas M. Evaluation of texture for classification of abdominal aortic aneurysm after endovascular repair. *J Digit Imag.* (2012) 25:369–76. doi: 10.1007/s10278-011-9417-7
24. Garcia G, Tapia A, De Blas M. Computer-supported diagnosis for endotension cases in endovascular aortic aneurysm repair evolution. *Comput Methods Programs Biomed.* (2014) 115:11–9. doi: 10.1016/j.cmpb.2014.03.004
25. Marschner CB, Kokla M, Amigo JM, Rozanski EA, Wiinberg B, McEvoy FJ. Texture analysis of pulmonary parenchymateous changes related to pulmonary thromboembolism in dogs - a novel approach using quantitative methods. *BMC Vet Res.* (2017) 13:219. doi: 10.1186/s12917-017-1117-1
26. Sullivan DC, Mirmalek-Sani SH, Deegan DB, Baptista PM, Aboushwareb T, Atala A, et al. Decellularization methods of porcine kidneys for whole organ engineering using a high-throughput system. *Biomaterials.* (2012) 33:7756–64. doi: 10.1016/j.biomaterials.2012.07.023
27. Szczypinski PM, Strzelecki M, Materka A. Mazda - a software for texture analysis. In: *Proceedings of the 2007 International Symposium on Information Technology Convergence (ISITC 2007)* (IEEE Computer Society) (2007). p. 245–9.
28. Szczypinski PM, Strzelecki M, Materka A, Klepaczko A. MaZda—a software package for image texture analysis. *Comput Methods Programs Biomed.* (2009) 94:66–76. doi: 10.1016/j.cmpb.2008.08.005
29. Strzelecki M, Szczypinski P, Materka A, Klepaczko A. A software tool for automatic classification and segmentation of 2D/3D medical images. *Nucl Instrum Methods Phys Res Sect A.* (2013) 702:137–40. doi: 10.1016/j.nima.2012.09.006
30. Maidman SD, Eberly LM, Greenbaum AB, Guyton RA, Wells BJ. Postinfarction ventricular septal rupture and hemopericardium with tamponade physiology. *CASE.* (2021) 5:48–50. doi: 10.1016/j.case.2020.10.010
31. Haralick RM, Shanmugam K, Dinstein I. Textural features for image classification. *IEEE Transact Syst Man.* (1973) 610–21. doi: 10.1109/TSMC.1973.4309314
32. Santos TA, Maistro CE, Silva CB, Oliveira MS, Franca Jr MC, et al. MRI texture analysis reveals bulbar abnormalities in friedreich ataxia. *AJNR Am J Neuroradiol.* (2015) 36:2214–8. doi: 10.3174/ajnr.A4455
33. Topalovic N, Mazic S, Nestic D, Vukovic O, Cunic J, Laketic D, et al. Association between chromatin structural organization of peripheral blood neutrophils and self-perceived mental stress: gray-level co-occurrence matrix analysis. *Microsc Microanal.* (2021) doi: 10.1017/S143192762101240X. [Epub ahead of print].
34. Kociolek M, Materka A, Strzelecki M, Szczypinski P. Discrete wavelet transform-derived features for digital image texture analysis. (2001).
35. Paunovic J, Vucevic D, Radosavljevic T, Vukomanovic Djurdjevic B, Stankovic S, Pantic I. Effects of iron oxide nanoparticles on structural organization of hepatocyte chromatin: gray level co-occurrence matrix analysis. *Microsc Microanal.* (2021) 27:889–96. doi: 10.1017/S1431927621000532
36. Ucci G, Danova M, Riccardi A, Brugnati S, Girino M, Corridoni S, et al. Abnormalities of T cell subsets in a patient with cyclic neutropenia. *Acta Haematol.* (1987) 77:177–9. doi: 10.1159/000205986
37. Hwang J, San BH, Turner NJ, White LJ, Faulk DM, Badylak SF, et al. Molecular assessment of collagen denaturation in decellularized tissues using a collagen hybridizing peptide. *Acta Biomaterialia.* (2017) 53:268–78. doi: 10.1016/j.actbio.2017.01.079
38. Schmitt A, Csiki R, Tron A, Saldamli B, Tubel J, Florian K, et al. Optimized protocol for whole organ decellularization. *Eur J Med Res.* (2017) 22:31. doi: 10.1186/s40001-017-0272-y
39. Periyah MH, Halim AS, Mat Saad AZ. Mechanism action of platelets and crucial blood coagulation pathways in hemostasis. *Int J Hematol Oncol Stem Cell Res.* (2017) 11:319–27.
40. Pantic I, Nestic Z, Paunovic Pantic J, Radojevic-Skodric S, Cetkovic M, Basta Jovanovic, G. Fractal analysis and gray level co-occurrence matrix method for evaluation of reperfusion injury in kidney medulla. *J Theor Biol.* (2016) 397:61–7. doi: 10.1016/j.jtbi.2016.02.038
41. Pantic I, Dacic S, Brkic P, Lavrnja I, Jovanovic T, Pantic S, et al. Discriminatory ability of fractal and grey level co-occurrence matrix methods in structural analysis of hippocampus layers. *J Theor Biol.* (2015) 370:151–6. doi: 10.1016/j.jtbi.2015.01.035
42. Zaletel I, Milutinović K, Bajčetić M, Nowakowski RS. Differentiation of amyloid plaques between Alzheimer's disease and non-alzheimer's disease individuals based on gray-level co-occurrence matrix texture analysis. *Microscopy Microanal.* (2021) 27:1146–53. doi: 10.1017/S1431927621012095
43. Pantic I, Pantic S. Germinal center texture entropy as possible indicator of humoral immune response: immunophysiology viewpoint. *Mol Imag Biol.* (2012) 14:534–40. doi: 10.1007/s11307-011-0531-1
44. Davidovic LM, Cunic J, Dugalic S, Vicentic S, Sevarac Z, Petroianu G, et al. Gray-level co-occurrence matrix analysis for the detection of discrete, ethanol-induced, structural changes in cell nuclei: an artificial intelligence approach. *Microsc Microanal.* (2022) 28:265–71. doi: 10.1017/s1431927621013878
45. Huang L, Feng B, Li Y, Liu Y, Chen Y, Chen Q, et al. Computed tomography-based radiomics nomogram: potential to predict local recurrence of gastric cancer after radical resection. *Front Oncol.* (2021) 11:638362. doi: 10.3389/fonc.2021.638362

46. Thuillier P, Bourhis D, Schick U, Alavi Z, Guezennec C, Robin P, et al. Diagnostic value of positron-emission tomography textural indices for malignancy of 18F-fluorodeoxyglucose-avid adrenal lesions. *Q J Nucl Med Mol Imag.* (2021) 65:79–87. doi: 10.23736/S1824-4785.19.03138-8
47. Khan HA, Shahzad MA, Iqbal F, Awan MA, Sharjeel M, Khan QA, et al. A novel method of quantifying the choriocapillaris in normal and post-inflammatory eyes. *Ocul Immunol Inflamm.* (2020) doi: 10.1080/09273948.2020.1800047. [Epub ahead of print].

**Conflict of Interest:** The authors declare that the research was conducted in the absence of any commercial or financial relationships that could be construed as a potential conflict of interest.

**Publisher's Note:** All claims expressed in this article are solely those of the authors and do not necessarily represent those of their affiliated organizations, or those of the publisher, the editors and the reviewers. Any product that may be evaluated in this article, or claim that may be made by its manufacturer, is not guaranteed or endorsed by the publisher.

Copyright © 2022 Pantic, Shakeel, Petroianu and Corridon. This is an open-access article distributed under the terms of the Creative Commons Attribution License (CC BY). The use, distribution or reproduction in other forums is permitted, provided the original author(s) and the copyright owner(s) are credited and that the original publication in this journal is cited, in accordance with accepted academic practice. No use, distribution or reproduction is permitted which does not comply with these terms.